FUDMA Journal of Sciences (FJS)
ISSN online: 2616-1370
ISSN print: 2645 - 2944
Vol. 10 No. 12, June, 2026, pp 38 – 44
DOI: https://doi.org/10.33003/fjs-2026-1012-5457

Integrated First-Principles Assessment of Cubic $SrHfO_3$: Elastic Stability, Harmonic Soft Modes and Ultraviolet Optical Response

***[1]Justine Madugu Sylvanus, [2]Jamu Yerima Benson and [2]Adam Usman**

[1]Department of Pure and Applied Physics, Adamawa State University, Mubi, Adamawa State, Nigeria
[2]Department of Physics, Modibbo Adama University, Yola, Adamawa State, Nigeria.

*Corresponding authors' email: madugu656@adsu.edu.ng
ORCID ID: 0009-0007-8797-5968

ABSTRACT
Cubic $SrHfO_3$ is a chemically robust wide-gap perovskite who's mechanical, vibrational and optical responses remain incompletely reconciled. In this study, we present a single-workflow integration of structural, electronic, elastic, vibrational, thermodynamic and optical density functional theory results for cubic $SrHfO_3$, bringing multiple property domains that are often treated separately into one internally consistent assessment. This integrated framework enabled the study to show, within one coherent analysis, that cubic $SrHfO_3$ is a stiff wide-gap and ultraviolet-active reference phase that is elastically stable but harmonically unstable at 0 K because of M- and R-point soft phonons. The optimised lattice constant is 4.0689 Å and the equilibrium (ev,x) equation-of-state bulk modulus is 175.70 GPa. The material is an indirect-gap insulator with a calculated R-to-Γ gap of 3.802 eV and a lowest direct gap of 4.143 eV at Γ; the valence edge is dominated by O 2p states and the conduction edge by Hf 5d states. The cubic elastic constants, C_{11} = 370.15 GPa, C_{12} = 78.21 GPa and C_{44} = 87.78 GPa, satisfy the Born criteria and give Hill averages B = 175.52 GPa, G = 107.74 GPa and E = 268.29 GPa. A B/G ratio of 1.63, negative Cauchy pressure and Zener factor of 0.601 indicate brittle, directionally bonded and anisotropic behaviour. In contrast to the elastic stability, imaginary phonons at M and R, reaching approximately -197.73 and -208.21 cm^{-1}, reveal 0 K antiferrodistortive instability of the ideal cubic lattice. The optical tensor is isotropic, with a low-energy electronic dielectric constant of about 4.37, an absorption onset near 4 eV and a maximum absorption coefficient of 1.65×10^6 cm^{-1} in the ultraviolet.

Received: 06 June 2026
Accepted: 07 July 2026
Published: 23 July 2026

Keywords: $SrHfO_3$; Density Functional Theory; Elastic Properties; Phonon Instability; Dielectric Function; Ultraviolet Absorption

INTRODUCTION

Oxide perovskites with the general formula ABO_3 provide a chemically flexible platform for coupling crystal symmetry, bond ionicity, electronic structure, lattice dynamics and dielectric response. The ideal cubic Pm-3m cell contains one formula unit, with the larger A-site cation in twelve-fold coordination, and the B-site cation at the centre of an oxygen octahedron. Even when this high-symmetry geometry is a useful computational reference, tolerance-factor arguments and first-principles studies show that many ABO_3 compounds lower their energy through octahedral rotation, polar displacement or other symmetry-breaking modes (Bartel et al., 2019; Lamichhane & Ravindra, 2021).

Strontium hafnate, $SrHfO_3$, is a closed-shell d^0 oxide in which the Sr^{2+} ion primarily stabilizes the A sublattice while the Hf–O network controls the near-gap electronic response. The compound is attractive as a chemically durable, wide-gap dielectric and as a host or precursor for optical, catalytic and electroceramic applications. Recent calculations on $SrHfO_3$ and related alkaline-earth hafnates consistently associate the upper valence states with O 2p orbitals and the lower conduction states with Hf 5d orbitals, but predicted lattice constants, gaps and optical onsets vary with the exchange-correlation treatment and structural model (Ahmed et al., 2022; 2020; Rehman et al., 2025). Comparable trends have also been reported for $CaHfO_3$, $BaHfO_3$ and alkaline-earth zirconates (Hoat et al., 2018; Lamichhane & Ravindra, 2021).

A particular methodological difficulty is that semilocal density functional approximations could reproduce equilibrium geometries reasonably well while underestimating excitation gaps and red-shifting calculated optical spectra (Ahmed et al., 2022; Borlido et al., 2020; Furness et al., 2020; Zulfiqar et al., 2021). Pseudopotential consistency, cutoff convergence and reproducible workflows are equally important for heavy-element oxides, especially when elastic constants and soft phonons are extracted from small energy or force differences (Giannozzi et al., 2017, 2020; Mazdziarz, 2024; Prandini et al., 2018; Talirz et al., 2020).

The available $SrHfO_3$ literature remains fragmented. Some studies emphasise structural and photocatalytic descriptors, others examine pressure-dependent optoelectronic or thermoelectric behaviour, while fewer combine equation-of-state, elastic, harmonic-phonon, thermodynamic and optical analyses within one workflow (Ahmed et al., 2022; Hasan et al., 2022). This fragmentation can obscure a central physical distinction: a cubic cell may satisfy the born elastic criteria while retaining unstable finite-wave-vector phonons.

In this study, we integrated the structural, electronic, elastic, vibrational, thermodynamic and optical results obtained for cubic $SrHfO_3$. The objectives were to: (i) establish the equilibrium geometry and bulk modulus; (ii) determine the band-edge locations and orbital character; (iii) test cubic mechanical stability, anisotropy and brittleness; (iv) identify harmonic soft modes and delimit the interpretation of derived thermodynamic functions; and (v) relate the dielectric and absorption spectra to the calculated O 2p to Hf 5d transitions. The central hypothesis is that the ideal cubic phase is a mechanically coherent but dynamically unstable high-symmetry reference structure, with strong ultraviolet rather than visible-light optical activity.

MATERIALS AND METHODS

Crystal Model and Electronic-Structure Framework

Calculations were carried out with Quantum ESPRESSO version 7.5 using a plane-wave projector-augmented-wave framework (Giannozzi et al., 2020). The exchange-correlation energy was treated with the PBEsol functional. The pseudopotentials were Sr.pbesol-spn-kjpaw_psl.1.0.0.UPF, Hf.pbesol-spn-kjpaw_psl.1.0.0.UPF and O.pbesol-nl-kjpaw_psl.1.0.0.UPF. The primitive cubic Pm-3m cell contained five atoms: Sr at (1/2, 1/2, 1/2), Hf at (0, 0, 0), and O at (0, 1/2, 0), (0, 0, 1/2) and (1/2, 0, 0). The non-spin-polarised unit cell contained 40 valence electrons.

The final electronic calculations used a 50 Ry wavefunction cutoff and a 500 Ry charge-density cutoff, together with a 12 × 12 × 12 Monkhorst-Pack mesh. Marzari-Vanderbilt smearing of 0.020 Ry was used during self-consistency and the total-energy threshold was 1.0×10^{-8} Ry. A separate cutoff scan and k-point scan were used to check the total-energy plateau. Curated pseudopotential and convergence practices followed the reproducibility principles discussed by Prandini et al. (2018) and Talirz et al. (2020).

Structural Relaxation and Equation of State

Variable-cell relaxation minimized the enthalpy with respect to cell dimensions and internal coordinates while preserving no imposed atomic displacement beyond the starting cubic symmetry. Static total-energy scans were then performed around the minimum. The refined energy-volume data were fitted with the Murnaghan equation of state to obtain the equilibrium volume V_O, minimum energy E_o, bulk modulus B_o and its pressure derivative B_o'.

$$H = E_{DFT} + P_{ext}V \quad (1)$$

$$V = a^3, P = \frac{-\partial E}{\partial V} \quad (2)$$

$$P(V) = \frac{B_o}{B_o'}\left[\left(\frac{V_o}{V}\right)^{B_o'} - 1\right] \quad (3)$$

Band Structure and Density of States

A self-consistent calculation at the optimised geometry generated the ground-state charge density. The band structure was sampled along Γ-X-M-R-Γ using 251 k points and 24 Kohn-Sham bands. Total and projected densities of states were evaluated with Gaussian broadening of 0.020 Ry. The band-edge character was assigned from the integrated orbital projections rather than from the dispersion alone.

$$\psi_{nk}(r) = e^{ik.r}u_{nk}(r) \quad (4)$$

$$D(E) = \sum_{n,k}\delta\big(E - E_n(k)\big) \quad (5)$$

$$E_g^{ind} = E_{CBM}(\Gamma) - E_{VBM}(R), E_g^{dir}(k) = E_c(k) - E_v(k) \quad (6)$$

Elastic, Vibrational and Thermodynamic Properties

The three independent cubic stiffness coefficients C_{11}, C_{12} and C_{44} were obtained from small-strain calculations. Mechanical stability was evaluated using $C_{11} - C_{12} > 0$, $C_{11} + 2C_{12} > 0$ and $C_{44} > 0$. Voigt and Reuss bounds were averaged to obtain the Hill bulk and shear moduli, from which Young's modulus, Poisson's ratio, the Pugh ratio, Zener anisotropy and the universal anisotropy index were derived.

$$B = (C_{11} + 2C_{12})/3 \quad (7)$$

$$G_V = (C_{11} - C_{12} + 3C_{44})/5 \quad (8)$$

$$G_R = 5(C_{11} - C_{12})\,C_{44}/[4C_{44} + 3(C_{11} - C_{12})] \quad (9)$$

$$E = 9BG/(3B + G), \nu = (3B - 2G)/[2(3B + G)] \quad (10)$$

Harmonic lattice dynamics were evaluated by density-functional perturbation theory and (DFPT) post-processed with the Quantum ESPRESSO/THERMO_PW workflow. The interatomic force constant (IFC) was computed on a coarse q−mesh **(**2×2×2) Monkhorst-Pack. Frequencies and eigenvectors along high-symmetry paths (Γ−X–M–Γ) were similarly calculated using matdyn.x in Quantum ESPRESSO. Being an insulator, born effective charges and dielectric tensors were added analytically to the dynamical matrix at q −> 0 before executing the interpolation.

The calculated phonon dispersion contains 3N = 3 × 5 = 15 modes as expected for a five-atom cell along the cubic high-symmetry path. Imaginary frequencies are reported as negative values. Debye and harmonic thermodynamic quantities were evaluated from the computed vibrational spectrum over approximately 0-800 K. The DFPT output used a 50 Ry wavefunction cutoff and a 500 Ry charge-density cutoff. Modern phonon methodology and the interpretation of imaginary modes follow Giustino (2017) and Togo et al. (2023). The phonon frequencies were obtained from the dynamical matrix through

$$det\left|D_{\alpha\beta}^{kk'}(q) - \omega^2(q)I\right| = 0 \quad (11)$$

Where $D_{\alpha\beta}^{kk'}(q)$ is the dynamical matrix at wave vector q, and ω (q) is the phonon frequency.

Dielectric and Optical Response

The complex electronic dielectric tensor was post-processed as $\varepsilon(\omega) = \varepsilon_1(\omega) + i\varepsilon_2(\omega)$. The refractive index n, extinction coefficient k, normal-incidence reflectivity R, absorption coefficient α and electron-energy-loss function L were derived from ε(ω) as described by Salihu et al. (2026). Cubic symmetry was verified from equality of the three diagonal components and vanishing off-diagonal components. Since the spectra were based on the underlying Kohn-Sham electronic structure, no quasiparticle, excitonic or temperature renormalisation correction was applied; the absolute optical threshold is therefore interpreted as semilocal-DFT (Ahmed et al., 2022; Borlido et al., 2020).

$$\tilde{N}(\omega) = n(\omega) + ik(\omega) \quad (12)$$

$$n = \left[\frac{\sqrt{\varepsilon_1^2+\varepsilon_2^2}+\varepsilon_1}{2}\right]^{\frac{1}{2}}, \; k = \left[\frac{\sqrt{\varepsilon_1^2+\varepsilon_2^2}-\varepsilon_1}{2}\right]^{\frac{1}{2}} \quad (13)$$

$$R(\omega) = \left|\frac{(\tilde{N}-1)}{(\tilde{N}+1)}\right|^2 = \frac{(n-1)^2+k^2}{(n+1)^2+k^2} \quad (14)$$

$$\alpha(\omega) = \frac{2\omega k(\omega)}{c} = \frac{4\pi k}{\lambda} \quad (15)$$

$$L(\omega) = -\Im[\varepsilon^{-1}(\omega)] \quad (16)$$

No stochastic sampling was involved. Numerical reliability was assessed from cutoff and k-point convergence, agreement among independent equilibrium-volume fits, and agreement between equation-of-state and elastic-tensor bulk moduli.

RESULTS AND DISCUSSION

Equilibrium Structure and Equation of State

The relaxed structure retained the ideal cubic atomic coordinates, indicating that the constrained five-atom cell lowered its energy mainly by homogeneous contraction rather than internal displacement. The variable-cell result gave a = 4.0645 Å, whereas the refined energy scan and Murnaghan fit converged to a_o = 4.0689 Å and V_o = 67.36 Å³. The difference between the relaxation and equation-of-state values is approximately 0.11%, demonstrating good internal consistency. The corresponding Hf−O distance is about 2.034 Å and the Sr−O distance about 2.877 Å.

The refined equation-of-state fit yielded B_o = 175.70 GPa and B_o' = 4.28. The energy-volume curve shows a single smooth minimum, while the pressure changes sign close to the fitted equilibrium volume (Figure 1). This bulk modulus identifies $SrHfO_3$ as a relatively incompressible oxide. It is also consistent with the strong Hf‒O framework expected in alkaline-earth hafnates and with the general trend that d^0 B-site octahedra dominate the resistance to hydrostatic compression (Ahmed et al., 2022).

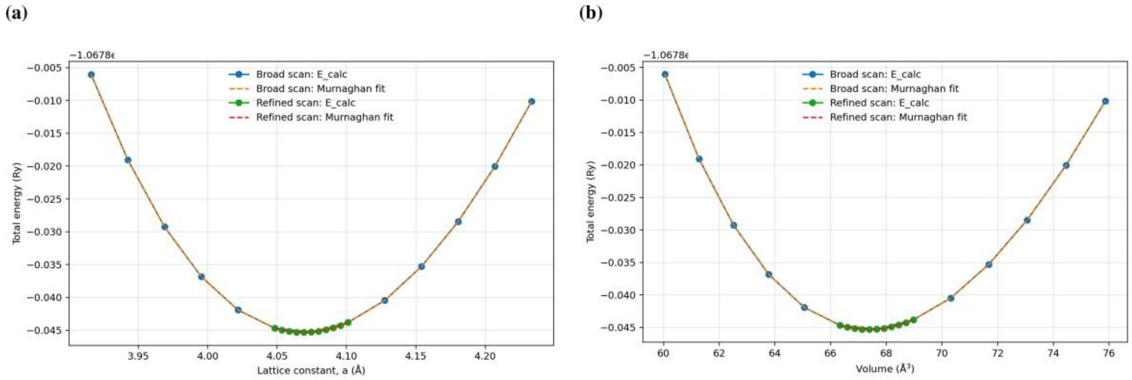

Figure 1: Equation-of-state of cubic $SrHfO_3$ (ev.x): (a) total energy as a function of lattice constant for broad and refined scans and (b) total energy as a function of unit-cell volume

The fitted minima define $a_o \approx 4.0689$ Å and $V_o \approx 67.36$ Å³.

Electronic Structure and Orbital Character

The band structure confirms that cubic $SrHfO_3$ is non-metallic. The valence-band maximum occurs at R and the conduction-band minimum at Γ, giving an indirect Kohn-Sham gap of 3.802 eV. The smallest direct gap is 4.143 eV at Γ (Figure 2). The 0.341 eV separations between the indirect and direct gaps imply that the first strong vertical optical transitions occur only slightly above the fundamental gap. This relationship is consistent with the calculated absorption onset near 4 eV.

The total DOS vanishes around the Fermi level and the integrated DOS plateaus at approximately 40 electrons, confirming complete filling of the valence manifold. The PDOS shows that the valence edge from -4 to 0 eV is approximately 95.6% O-derived, whereas the 0-4 eV conduction window is approximately 83.1% Hf-derived. The dominant low-energy excitation is therefore O 2p to Hf 5d. The small Hf contribution in the upper valence band and O contribution in the lower conduction band indicate finite Hf-O covalence superimposed on a largely ionic Sr^{2+} $-Hf^{4+}-O^{2-}$ framework. Sr contributes only weakly near the band edges and acts primarily as the A-site structural cation.

The calculated gap is in the range expected from semilocal descriptions of a wide-gap hafnate but should not be treated as a quasiparticle gap. Ahmed et al. (2022) showed that SCAN-based structural optimisation combined with a band-gap-improving potential substantially changes the $SrHfO_3$ optical threshold. The present gap is therefore most reliable for classifying the material and comparing internal trends.

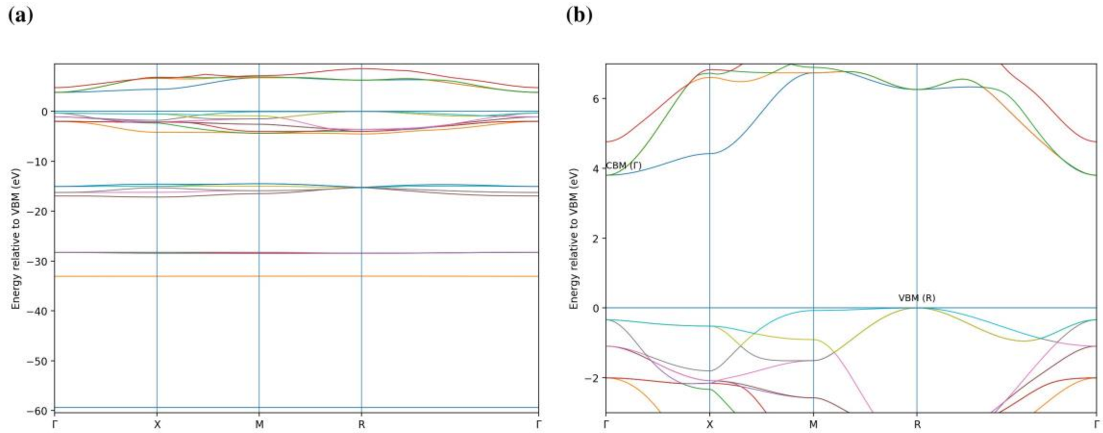

Figure 2: Electronic band structure of cubic $SrHfO_3$ along Γ-X-M-R-Γ: (a) full calculated energy range and (b) enlarged band-edge region

The valence-band maximum is at R and the conduction-band minimum at Γ, giving an indirect gap of 3.802 eV.

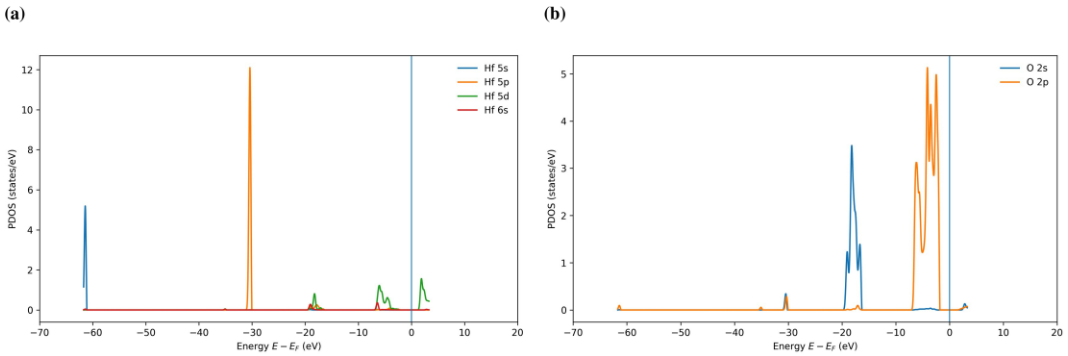

Figure 3: Orbital-projected densities of states of cubic $SrHfO_3$: (a) Hf projections, showing dominant Hf 5d weight at the conduction edge, and (b) O projections, showing dominant O 2p weight at the valence edge Energies are referenced to the Fermi level

Elastic Stability, Brittleness and Anisotropy

The calculated elastic constants are C_{11} = 370.15 GPa, C_{12} = 78.21 GPa and C_{44} = 87.78 GPa. All cubic Born criteria are satisfied: $C_{11} - C_{12}$ = 291.94 GPa, $C_{11} + 2C_{12}$ = 526.57 GPa and $C_{44} > 0$. The constrained cubic cell is therefore mechanically stable against infinitesimal homogeneous strain. The bulk modulus calculated directly from the elastic tensor, $(C_{11} + 2C_{12})/3$ = 175.52 GPa, differs from the equation-of-state value by only 0.10%, providing a strong internal consistency check.

The Voigt-Reuss-Hill shear modulus is 107.74 GPa and the corresponding Young's modulus is 268.29 GPa. These values confirm a stiff ceramic response. The Pugh ratio B/G = 1.63 lies below the conventional ductile-brittle threshold of 1.75, while the Poisson ratio is 0.245. Both indicators place cubic $SrHfO_3$ on the brittle side of the empirical classification. The Cauchy pressure $C_{11} - C_{44}$ = -9.57 GPa further suggests directional Hf–O bonding rather than a metallic-like central-force response.

The Zener anisotropy factor $A = 2C_{44}/(C_{11} - C_{12})$ is 0.601, and the universal anisotropy index is approximately 0.317. Thus, despite cubic symmetry, the single-crystal shear response is appreciably direction dependent. This distinction matters when extrapolating polycrystalline averages to textured films, oriented grains or stress-driven phase transformations.

Harmonic Phonons and Thermodynamic Response

The phonon spectrum contains three acoustic and twelve optical branches, as required for the five-atom primitive cell. The acoustic branches approach zero at Γ, but pronounced imaginary modes occur at the zone-boundary M and R points. The lowest frequencies are approximately -196.73 cm^{-1} at M and -208.21 cm^{-1} at R, the latter triply degenerate (Figure 4). Because the instability is strongest at finite wave vector rather than Γ, it is most naturally associated with antiferrodistortive rotations or tilts of neighbouring HfO_6 octahedra rather than a simple zone-centre polar displacement.

This result resolves an apparent contradiction. The elastic tensor proves stability against uniform strain, whereas the phonons reveal instability against a modulated internal displacement. Related first-principles studies of perovskites have similarly shown that high-symmetry phases can be meaningful average structures despite harmonic soft modes (Lamichhane & Ravindra, 2021; Togo et al., 2023).

The positive-frequency spectrum extends to approximately 938 cm^{-1} and contains a large gap between lower modes and the high-frequency oxygen-stretching block. The harmonic zero-point energy is 0.2596 eV per cell. At 300 K, the phonon-derived heat capacity is about 89.1 J mol^{-1} K^{-1}, while the Debye model gives about 108.2 J mol^{-1} K^{-1}. The Debye temperature lies between 514.8 and 517.9 K depending on whether it is inferred from the thermodynamic fit or elastic sound velocity. By 799 K, the Debye heat capacity reaches approximately 122.2 J mol^{-1} K^{-1}, close to the Dulong-Petit limit of 15R = 124.7 J mol^{-1} K^{-1} (Figure 5).

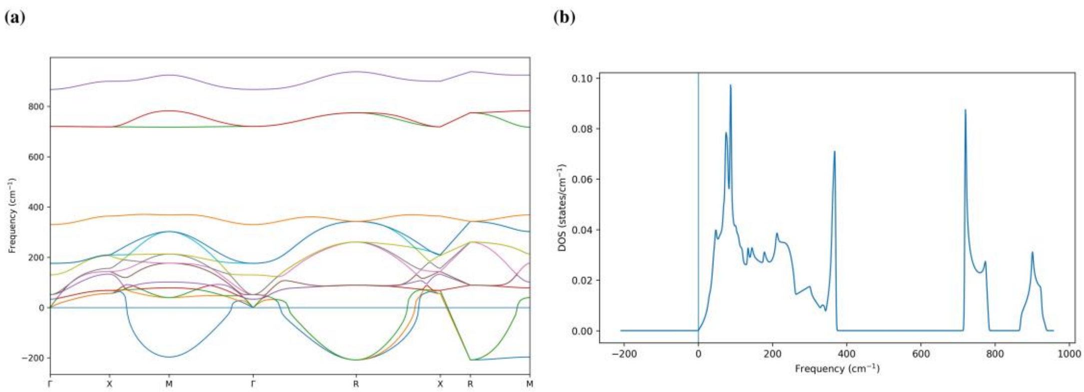

Figure 4: Lattice dynamics of cubic $SrHfO_3$: (a) phonon dispersion showing imaginary modes at M and R and (b) phonon density of states

Negative frequencies denote unstable harmonic modes of the ideal Pm-3m reference phase.

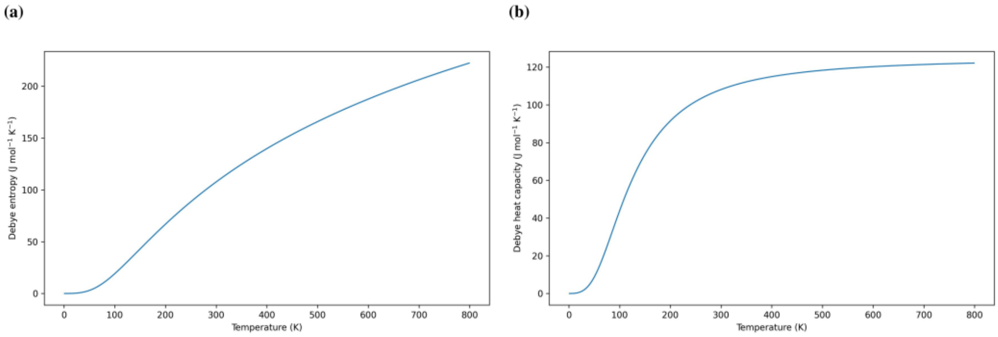

Figure 5: Debye thermodynamic functions of cubic $SrHfO_3$: (a) entropy and (b) constant-volume heat capacity

The heat capacity approaches the five-atom Dulong-Petit limit at high temperature.

Dielectric Function and Optical Response

The dielectric tensor is isotropic within numerical precision, as required by the cubic reference symmetry. The low-energy electronic dielectric constant is approximately 4.37, corresponding to a refractive index of about 2.09. The imaginary dielectric function remains negligible at low energy and rises strongly at approximately 3.9-4.1 eV, consistent with the lowest direct electronic transition. The real part reaches 7.29 at 5.58 eV and crosses zero near 11.28 and 13.75 eV, while the principal loss peak occurs at 13.89 eV (Figure 6).

The refractive index reaches 2.83 at 6.43 eV and the extinction coefficient reaches 1.74 at 7.28 eV (Figure 7). The maximum normal-incidence reflectivity is modest, about 0.338 at 7.07 eV. In contrast, the absorption coefficient rises to 1.65×10^6 cm^{-1} near 11.33 eV (Figure 8), demonstrating strong far-ultraviolet absorption. The spectral assignment is consistent with transitions from O 2p valence states into Hf 5d conduction states.

The calculated transparency below approximately 4 eV and strong ultraviolet absorption suggest possible use as a UV-active dielectric or protective optical material rather than a visible-light absorber. The relative ordering, isotropy and dominant ultraviolet character are robust.

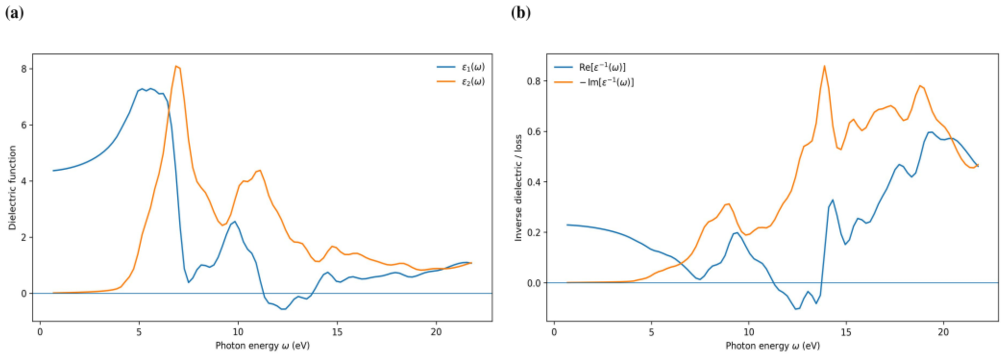

Figure 6: Optical response of cubic $SrHfO_3$: (a) real and imaginary parts of the complex dielectric function and (b) real inverse dielectric function with the energy-loss function

The response is isotropic for the cubic reference phase.

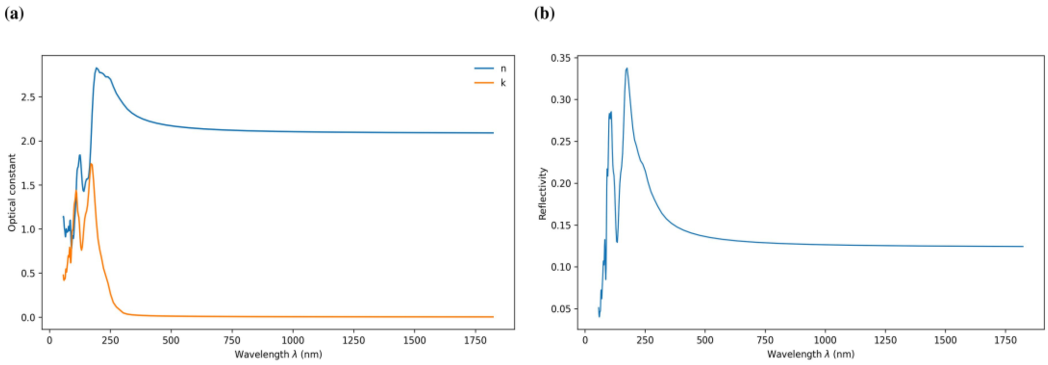

Figure 7**:** Wavelength-dependent optical constants of cubic $SrHfO_3$: (a) refractive index and extinction coefficient and (b) reflectivity spectrum

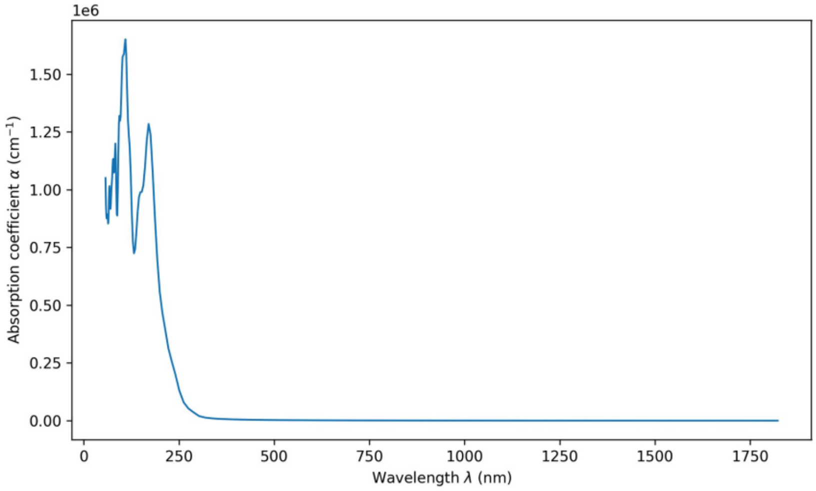

Figure 8: Calculated absorption coefficient of cubic $SrHfO_3$ as a function of wavelength
The strongest absorption occurs in the ultraviolet, reaching approximately 1.65×10^6 cm^{-1}.

CONCLUSION

An integrated PBEsol-DFT assessment of the ideal cubic $SrHfO_3$ perovskite has been developed from structural, electronic, elastic, vibrational, thermodynamic and optical calculations. The equilibrium lattice constant is 4.0689 Å and the bulk modulus is approximately 176 GPa. $SrHfO_3$ is an indirect-gap insulator with an R-to-Γ Kohn-Sham gap of 3.802 eV, an O 2p valence edge and an Hf 5d conduction edge. Its elastic tensor satisfies the cubic born criteria and predicts a stiff, moderately anisotropic and brittle solid.

The most important finding is that elastic stability does not imply dynamical stability. Strong imaginary M- and R-point phonons show that the ideal Pm-3m lattice is unstable in the 0 K harmonic approximations. The isotropic optical response exhibits a near-4 eV onset and strong ultraviolet absorption.

REFERENCES

Ahmed, S., Zulfiqar, W., Javed, F., Arshad, H., Abbas, G., Laref, A., & Alay-e-Abbas, S. M. (2022). Accurate first-principles evaluation of structural, electronic, optical and photocatalytic properties of $BaHfO_3$ and $SrHfO_3$ perovskites. Journal of Alloys and Compounds, 892. https://www.sciencedirect.com/science/article/pii/S0925838821034800

Bartel, C. J., Sutton, C., Goldsmith, B. R., Ouyang, R., Musgrave, C. B., Ghiringhelli, L. M., & Scheffler, M. (2019). New tolerance factor to predict the stability of perovskite oxides and halides. Science Advances, 5(2), eaav0693. https://doi.org/10.1126/sciadv.aav0693

Borlido, P., Schmidt, J., Huran, A. W., Tran, F., Marques, M. A. L., & Botti, S. (2020). Exchange-correlation functionals for band gaps of solids: Benchmark, reparametrization and machine learning. npj Computational Materials, 6, Article 96. https://doi.org/10.1038/s41524-020-00360-0

Furness, J. W., Kaplan, A. D., Ning, J., Perdew, J. P., & Sun, J. (2020). Accurate and numerically efficient r²SCAN meta-generalized gradient approximation. The Journal of Physical Chemistry Letters, 11(19), 8208-8215. https://doi.org/10.1021/acs.jpclett.0c02405

Giannozzi, P., Andreussi, O., Brumme, T., Bunau, O., Buongiorno Nardelli, M., Calandra, M., Car, R., Cavazzoni, C., Ceresoli, D., Cococcioni, M., Colonna, N., Carnimeo, I., Dal Corso, A., de Gironcoli, S., Delugas, P., DiStasio, R. A., Jr., Ferretti, A., Floris, A., Fratesi, G., Fugallo, G., Gebauer, R., Gerstmann, U., Giustino, F., Gorni, T., Jia, J., Kawamura, M., Ko, H.-Y., Kokalj, A., Küçükbenli, E., Lazzeri, M., Marsili, M., Marzari, N., Mauri, F., Nguyen, N. L., Nguyen, H.-V., Otero-de-la-Roza, A., Paulatto, L., Poncé, S., Rocca, D., Sabatini, R., Santra, B., Schlipf, M., Seitsonen, A. P., Smogunov, A., Timrov, I., Thonhauser, T., Umari, P., Vast, N., Wu, X., & Baroni, S. (2017). Advanced capabilities for materials modelling with Quantum ESPRESSO. Journal of Physics: Condensed Matter, 29(46), 465901. https://doi.org/10.1088/1361-648X/aa8f79

Giannozzi, P., Baseggio, O., Bonfà, P., Brunato, D., Car, R., Carnimeo, I., Cavazzoni, C., de Gironcoli, S., Delugas, P., Ferrari Ruffino, F., Ferretti, A., Marzari, N., Timrov, I., Urru, A., & Baroni, S. (2020). Quantum ESPRESSO toward the exascale. The Journal of Chemical Physics, 152(15), 154105. https://doi.org/10.1063/5.0005082

Giustino, F. (2017). Electron-phonon interactions from first principles. Reviews of Modern Physics, 89(1), 015003. https://doi.org/10.1103/RevModPhys.89.015003

Hasan, M., Nasrin, S., Islam, M. N., & Hossain, A. K. M. (2022). First-principles insights into the electronic, optical, mechanical, and thermodynamic properties of lead-free cubic ABO_3 perovskites. AIP Advances, 12(8), 085327. https://doi.org/10.1063/5.0104191

Hoat, D. M., Silva, J. F. R., & Blas, A. M. (2018). First-principles study of structural, electronic and optical properties of perovskites $CaZrO_3$ and $CaHfO_3$ in cubic phase. Solid State Communications. https://www.sciencedirect.com/science/article/pii/S0038109818300887

Lamichhane, A., & Ravindra, N. M. (2021). First-principles study of cubic alkaline-earth metal zirconate perovskites. Journal of Physics Communications. https://doi.org/10.1088/2399-6528/abe9fd

Mazdziarz, M. (2024). Uncertainty of DFT calculated mechanical and structural properties of solids due to incompatibility of pseudopotentials and exchange-correlation functionals. Journal of Chemical Theory and Computation. https://doi.org/10.1021/acs.jctc.4c01036

Prandini, G., Marrazzo, A., Castelli, I. E., Mounet, N., & Marzari, N. (2018). Precision and efficiency in solid-state pseudopotential calculations. npj Computational Materials, 4, Article 72. https://doi.org/10.1038/s41524-018-0127-2

Rehman, A., Abid, M. B., & Esa, F. B. (2025). DFT study of $SrHfO_3$ and $SrHf_{0.88}Ce_{0.11}O_3$ perovskites: Structural stability, electronic and optical properties, elasto-mechanical behavior, and photocatalytic performance. Journal of Electronic Materials. https://doi.org/10.1007/s11664-024-11698-2

Salihu. I. K., Yakubu, A., Aliero, Y. A., & Abdullahi, S. (2026). First-principles investigation of the electronic and optical properties of tin chalcogenides (SnS, SnSe and SnTe) using density functional theory. *FUDMA Journal of Sciences*, *10*(ANB-K Special Issue), pp 97. https://doi.org/10.33003/fjs-2026-10(ANB-K)-5321

Talirz, L., Kumbhar, S., Passaro, E., Yakutovich, A. V., Granata, V., Gargiulo, F., Borelli, M., Uhrin, M., Huber, S. P., Zoupanos, S., Adorf, C. S., Andersen, C. W., Schütt, O., Pignedoli, C. A., Passerone, D., VandeVondele, J., Schulthess, T. C., Smit, B., Pizzi, G., & Marzari, N. (2020). Materials Cloud, a platform for open computational science. Scientific Data, 7, 299. https://doi.org/10.1038/s41597-020-00637-5

Togo, A., Chaput, L., Tadano, T., & Tanaka, I. (2023). Implementation strategies in phonopy and phono3py. Journal of Physics: Condensed Matter, 35, 353001. https://doi.org/10.1088/1361-648X/acd831

Zulfiqar, W., Alay-e-Abbas, S. M., Abbas, G., Laref, A., Larsson, J. A., & Shaukat, A. (2021). Revisiting the structural, electronic and photocatalytic properties of Ti- and Zr-based perovskites with meta-GGA functionals of DFT. Journal of Materials Chemistry C. https://doi.org/10.1039/D0TC05964A